

Superpixel segmentations for thin sections: evaluation of methods to enable the generation of machine learning training data sets

Jiaxin Yu^a, Florian Wellmann^{a,*}, Simon Virgo^{a,e}, Marven von Domarus^d, Mingze Jiang^{a,b}, Joyce Schmatz^{b,c}, Bastian Leibe^d

^a*RWTH-Aachen, Geoscience, Department of Computational Geoscience and Reservoir Engineering, Germany*

^b*MaP Microstructure and Pores GmbH, Germany*

^c*RWTH-Aachen, Lehr- und Forschungsgebiet für Geologie-Endogene Dynamik, Germany*

^d*RWTH-Aachen, Visual Computing Institute, Computer Vision group, Germany*

^e*Terranigma Solutions GmbH, Germany*

This manuscript has been submitted for publication in **Computers & Geosciences**. The paper has **not yet undergone peer-review**. Subsequent versions of this manuscript may have slightly different content. If accepted, the final version of this manuscript will be available via the ‘Peer-reviewed Publication DOI’ link on the right-hand side of this webpage. Please feel free to contact any of the authors; we welcome feedback.

*Corresponding author

Email address: `florian.wellmann@cgre.rwth-aachen.de`, `@flohorovicic` (Florian Wellmann)

Superpixel segmentations for thin sections: evaluation of methods to enable the generation of machine learning training data sets

Jiaxin Yu^a, Florian Wellmann^{a,*}, Simon Virgo^{a,e}, Marven von Domarus^d, Mingze Jiang^{a,b}, Joyce Schmatz^{b,c}, Bastian Leibe^d

^a*RWTH-Aachen, Geoscience, Department of Computational Geoscience and Reservoir Engineering, Germany*

^b*MaP Microstructure and Pores GmbH, Germany*

^c*RWTH-Aachen, Lehr- und Forschungsgebiet für Geologie-Endogene Dynamik, Germany*

^d*RWTH-Aachen, Visual Computing Institute, Computer Vision group, Germany*

^e*Terranigma Solutions GmbH, Germany*

Abstract

Training data is the backbone of developing either Machine Learning (ML) models or specific deep learning algorithms. The paucity of well-labeled training image data has significantly impeded the applications of ML-based approaches, especially the development of novel Deep Learning (DL) methods like Convolutional Neural Networks (CNNs) in mineral thin section images identification. However, image annotation, especially pixel-wise annotation is always a costly process. Manually creating dense semantic labels for rock thin section images has been long considered as an unprecedented challenge in view of the ubiquitous variety and complexity of minerals in thin sections. To speed up the annotation, we propose a human-computer collaborative pipeline in which superpixel segmentation is used as a boundary extractor to avoid hand delineation of instances boundaries. The pipeline consists of two steps: superpixel segmentation using MultiSLIC, and superpixel labeling through a specific-designed tool. We use a cutting-edge methodology Virtual Petroscopy (ViP) for automatic image acquisition. Bentheimer sandstone sample is used to conduct performance testing of the pipeline. Three standard error metrics are used to evaluate the performance of Mul-

*Corresponding author

Email address: `florian.wellmann@cgre.rwth-aachen.de` (Florian Wellmann)

tiSLIC. The result indicates that MultiSLIC is able to extract compact superpixels with satisfying boundary adherence given multiple input images. According to our test results, large and complex thin section images with pixel-wisely accurate labels can be annotated with the labeling tool more efficiently than in a conventional, purely manual work, and generate data of high quality.

Keywords: Mineral thin section images, Pixel-wise labeling, Image annotation, Superpixel segmentation

1. Introduction

The analysis of petrographic thin sections is a standard process in many geological and mineralogical studies. Traditionally, this analysis relies highly on the visual interpretation by experts through petrographic microscopes, and this aspect will remain important, as it allows to integrate wide-ranging expertise, different microscopic techniques, and the geological context of the investigated material. However, this conventional approach is time-consuming and therefore limited to selected samples. As geological surveys, resource companies and research institutes are increasingly digitizing petrographic thin sections, approaches for an automated quantitative analysis are now becoming a standard tool to investigate properties in thin sections (e.g. [Marmo et al., 2005](#); [Singh et al., 2010](#); [Młynarczyk et al., 2013](#); [Thompson et al., 2001](#); [Baykan and Yilmaz, 2010](#); [Borges and de Aguiar, 2019](#); [Ramil et al., 2018](#); [Maitre et al., 2019](#)). These approaches have been driven by the rapid developments in the field of visual image analysis and segmentation leading to considerable progress in computer-aided methods for the automated analysis of mineral thin section images.

Currently, most of these approaches are based on supervised classification methods, where a training data set, generated by human experts, is used as an input to train a machine learning model for subsequent prediction of other samples. In the specific case of visual object detection, this process is referred to as image annotation. Image annotation can be done at three levels, namely image-wise tagging ([Deng et al., 2009](#); [Krasin et al., 2017](#)), object-wise segmentation ([Lin](#)

19 et al., 2014; Netzer et al., 2011) and pixel-wise labeling (Lin et al., 2014; Everingham et al.
20 2010). According to the level of annotation in the training data set, the subsequent machine
21 learning models can be classified into image categorization, mineral identification, and pixel-based
22 segmentation.

- 23 • In image classification (Fig. 1a), the input is usually a tagged image while the goal is to
24 predict the correct class label of the entire image. In the case of petrographic thin section
25 analyses, class labels are usually referring to lithology, rock type or texture (e.g. Marmo
26 et al., 2005; Młynarczuk et al., 2013; Singh et al., 2010).
- 27 • In mineral identification (Fig. 1b), a classifier is trained on top of images where target
28 mineral grains are manually identified ahead of time. The output is usually a segmentation
29 map where each type of mineral is indicated by a unique color-mode (Budenny et al.
30 2017; Thompson et al., 2001; Baykan and Yılmaz, 2010; Borges and de Aguiar, 2019; Ramil
31 et al., 2018). Compared to image tagging, generating training sets for grain segmentation
32 and identification is more time-consuming, as it requires a detailed mineral detection and
33 identification process.
- 34 • A full segmentation of thin sections (Fig. 1c) requires a detailed tracing of grain boundaries.
35 The recent success of deep convolutional neural networks (CNNs) (Krizhevsky et al., 2012;
36 Szegedy et al., 2015) has empowered the development of semantic segmentation (Long et al.,
37 2015) using automatic feature hierarchy extraction (Long et al., 2015; Lin et al., 2016). First
38 approaches using CNNs for mineral thin section analysis have been reported by Cheng and
39 Guo (2017); Iglesias et al. (2019); Karimpouli and Tahmasebi (2019); Tang et al. (2017).

40 With the potential to consider both local (e.g. optical characteristics of mineral) and contex-
41 tual information (rock texture and structure), full segmentation approaches are very promising
42 for large-scale thin section analysis, with a potential to approach human-level analysis. At the

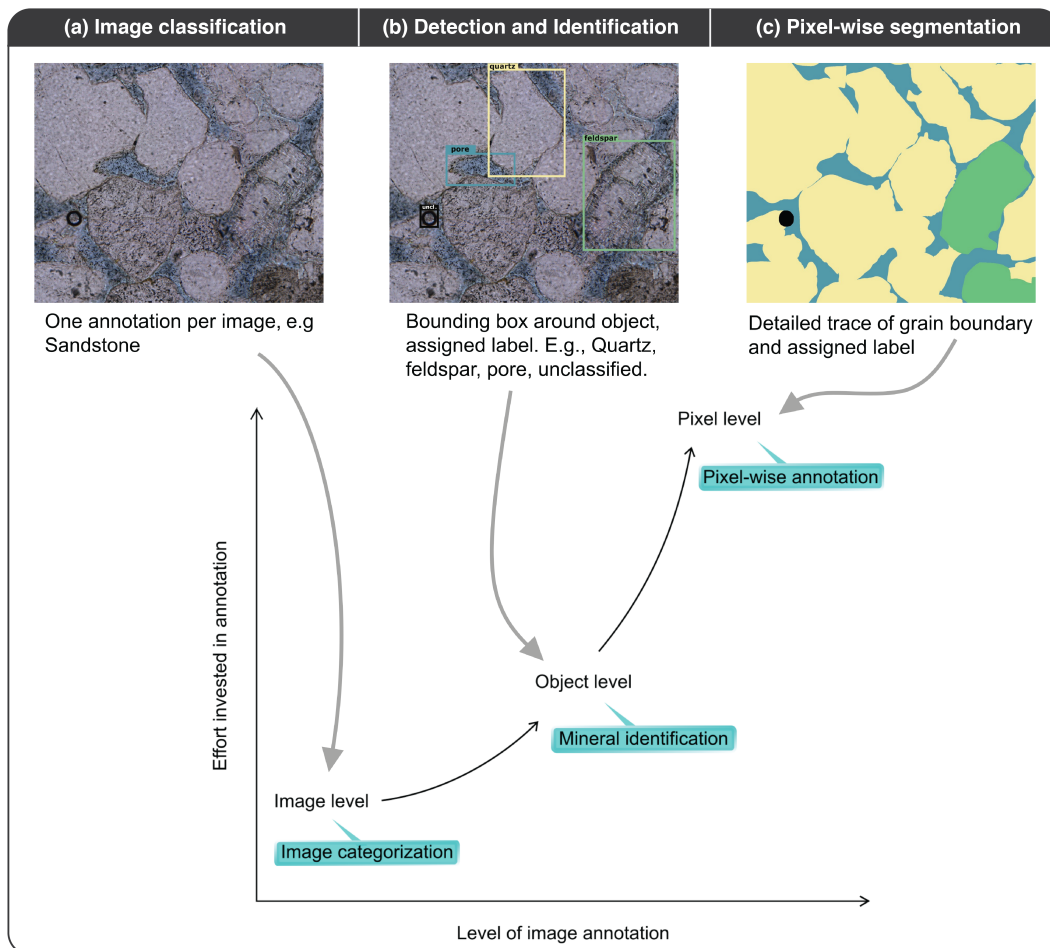


Figure 1: Illustration of the relationship between the level of annotation and required human intervention

43 same time, deep learning models also place higher requirements on data annotation (Sun et al.
44 2018), as most widely used CNN structures (Ronneberger et al., 2015; Krizhevsky et al., 2012
45 He et al., 2016; Simonyan and Zisserman, 2014) require a large amount of well-labeled categorical
46 labels from images. In computer vision, the stunning achievements of machine learning and deep
47 learning applications are strongly motivated by many large-scale open-source data sets such as
48 MSCOCO (Lin et al., 2014), Cityscapes (Cordts et al., 2016) and LabelMe (Russell et al., 2008).
49 Well annotated data sets are being used not only to learn classifiers, but to reliably identify and
50 evaluate the promising methods (Hradiš et al., 2012). In the field of petrographic thin section
51 analyses, such a large annotated data set is not yet available. And as sketched in Fig. 1, a label-
52 ing of image domains and grain boundaries requires detailed and careful line draws—a work that
53 quickly becomes infeasible for large thin section data sets. It is also worth noting that labeling of
54 petrographic thin sections is a highly specialized task that cannot be outsourced easily to labeling
55 services: whereas it is possible for almost everyone to identify a traffic light in an image (e.g.
56 Von Ahn et al., 2004), separating quartz from feldspar in a thin section requires specific training
57 and expertise.

58 To overcome the problem of limited data sets for thin section analysis, previous approaches
59 used pre-trained models using the principle of transfer learning (e.g. Zhang et al., 2019) or data
60 augmentation (e.g. Karimpouli and Tahmasebi, 2019). However, these approaches are also limited,
61 as minerals in thin sections show specific characteristics that are different to most of the images in
62 classical data sets (for example those mentioned above) and the transfer is therefore limited. Also,
63 even if augmentation methods can successfully be used to obtain more robust classification results,
64 the possibility to identify features is still limited to the variability in the initial (small) data set.

65 Based on these preliminary considerations, we derive the premise that fully labeled data sets
66 of thin sections are required to evaluate the full potential of novel machine learning algorithms.
67 However, we also need methods to facilitate labeling by experts, making specific use of the char-
68 acteristics in thin sections.

69 In this context, we propose the idea that such a data set including high-quality pixel-wise
70 labels could be efficiently obtained through a human-computer collaborative annotation pipeline
71 where computers extract grain boundaries by splitting images into superpixels. These superpixels
72 are groups of pixels with similar properties and commonly determined with through unsupervised
73 learning algorithms (e.g. [Ren and Malik, 2003](#); [Stutz et al., 2018](#)). In this paper, we first evaluate
74 commonly used superpixel methods for their compatibility with the specific requirements to label
75 petrographic thin sections. For this aim, we also revisit different evaluation measures.

76 One limitation of the existing algorithms is that they are designed for image data and therefore
77 cannot consider all information from thin section data sets with plain-polarised and cross-polarized
78 light images at multiple polarization angles. We address this issue with the extension of one of the
79 most promising methods, SLIC, and propose a novel algorithm, MultiSLIC, that enables superpixel
80 generation with multiple channels.

81 The paper is organised as follows: section [2](#) introduces the principles behind digital thin section
82 generation and the dataset used in the following experiments. In section [3](#), we present the concept
83 of superpixel segmentation in an image annotation pipeline and compare the existing segmentation
84 algorithms. In addition, we present an own extension to consider multiple input channels, as these
85 are often available for thin section data (for example when plane-polarized and cross-polarized
86 images are available). In section [4](#), we present the results of a quantitative evaluation of these
87 superpixel algorithms in the application to a real thin section and finally provide considerations
88 for practical use in section [5](#).

89 **2. Digital petrographic thin section data**

90 **2.1. Digital petrography**

91 The variation of optical features of a mineral under different settings of a petrographic mi-
92 croscope is closely related to crystallographic characteristics that can be indicative of the mineral

93 (e.g. MacKenzie et al. 2017). In order to fully capture optical features in digital images, we use
94 here a Virtual Petrography (ViP) system developed by Fraunhofer FIT in collaboration with the
95 Institute of Structural Geology, Tectonics and Geomechanics at RWTH Aachen University (Virgo
96 et al. 2016). The system is able to fully capture the information of entire rock thin-sections in a
97 digital format under different settings, including objective zooming, stage rotation, and switching
98 between plane polarized light (ppol) and crossed polarized light (xpol) (Virgo et al. 2016). The
99 hardware of the system is an automated petrographic microscope that scans the thin sections in
100 high resolution (up to 10^9 pixels per square centimeter with a 40x objective). The scanning process
101 is performed sequentially along a predefined grid and automatically repeated for different rotation
102 angles of crossed polarizers. Each scanned mosaic patch is an RGB image with 384 x 520 pixels,
103 and patches are then seamlessly stitched to obtain a full thin section image. For a typical thin
104 section with a size of 3 cm by 2 cm and a zoom level of 10x, we obtain a stitched image of 86,960
105 x 57,970 pixels.

106 High-resolution images at different rotation angles can be precisely matched on a pixel-level.
107 This matching allows to determine the extinction behaviour at each pixel location, which can be
108 interpolated with a smoothed function to compress information (Virgo et al. 2016). Based on
109 the interpolated extinction information, a phase map can be produced to qualitatively show the
110 mineral axis misorientations. This specific system also contains a dedicated displaying toolbox
111 to allow users to adjust colouring of images and to evaluate extinction angles and behaviour. As
112 shown in Fig. 2a, multiple scanning image layers form a digital thin section cube that captures
113 the full optical characteristics of a thin section viewed under various polarisation and illumination
114 conditions.

115 2.2. Thin section data set

116 The sample data set used in the paper is Bentheimer Sandstone (BS), which is one of the most
117 well-known sandstone types in Europe. Locations with outcrops of this sandstone can be found

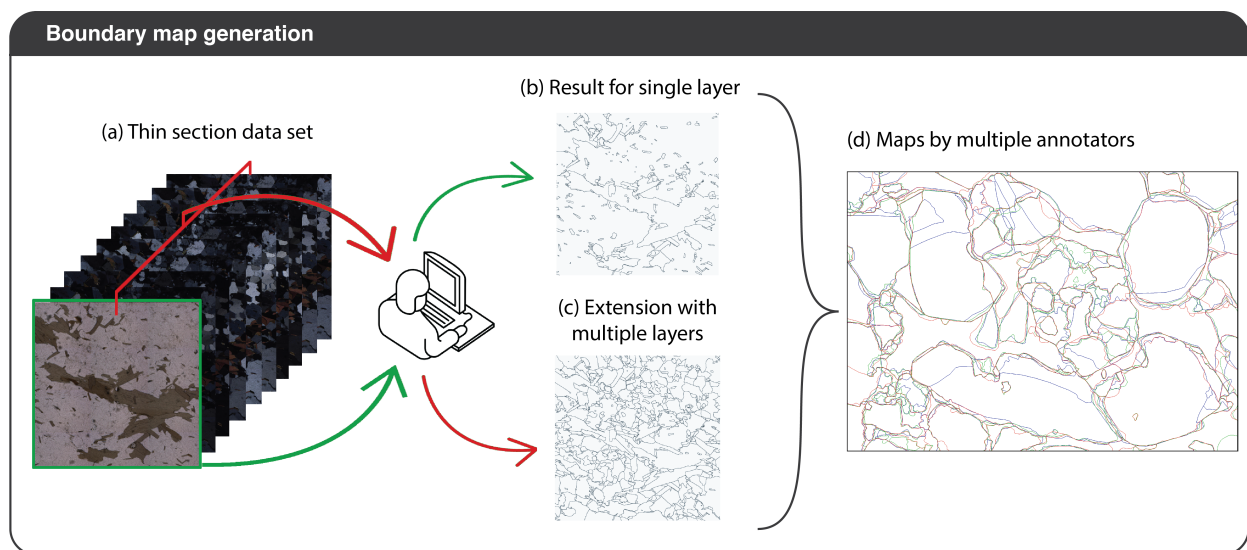


Figure 2: Ground-truth generation for digital thin section. (a) Ppol and all xpol layers form the labeling ground. (b) incomplete contour map generated based on a single layer in the image stack, in contrast, (c) shows the desired result containing the full shape of grains using the methodical approach; (d) Boundary maps delineated by different human annotators

118 on the border between the Netherlands and Germany. It forms a significant reservoir rock for
119 petroleum reservoirs and is characterized by loose compaction, simple mineral composition and a
120 well-sorted grain and pore space network (Peksa et al., 2015). The sandstone is mainly composed
121 of loosely packed detrital quartz grains, with additional 2-4% of altered Feldspar. Due to its
122 properties and the block-scale homogeneity and lateral continuity, this rock type is widely used as
123 a standard reservoir analogue. In the following, we use a sample of this sandstone which has some
124 detrital chert fragments, which appear as speckled grain composed of coarsely crystalline quartz.
125 Pores in the sample were impregnated with light blue-dyed epoxy resin.

126 2.3. Generating boundary maps for digital thin sections

127 Evaluating the quantitative performance of superpixel segmentations for a digital thin section
128 (ViP data set) requires a ground truth, which is manually generated by an expert. In order to
129 obtain comparable ground truth maps from multiple experts, we devised a tracing plan for the
130 procedure to reduce a potential procedural bias. The detailed tracing plan consists of four steps:

- 131 1. Prepare a ground-truth layer in tracing software (for example QGIS, vector graphics pro-
132 gramme);
- 133 2. Start from one of the image layers and trace all clearly visible boundaries;
- 134 3. Go to the next image layer and trace new boundaries that emerged;
- 135 4. Repeat the step 3 until all image layers are utilized. Note that, none of the boundaries that
136 have been traced according to the previous layer will be deleted or modified when going to
137 the next layer.

138 An example of this procedure is shown in Fig. 2 given a digital thin section data set with
139 one ppol and multiple xpol layers corresponding to different polarization angles (a), boundaries in
140 every layer are sequentially traced to obtain one single ground truth. Fig. 2(b) shows an incomplete
141 boundary map, with boundaries traced on the ppol layer. In contrast, Fig. 2(c) represents the

142 complete boundary map that includes all boundary information obtained from all image layers.
143 As shown in Fig. 2(d), three different ground truth boundary maps are generated by three different
144 domain experts to average the human bias. These boundary maps are subsequently used as ground
145 truths for a quantitative superpixel evaluation in section 4. As there are three outputs for each
146 error metric given three ground truth maps, the final quantitative results are averages of the three
147 outputs.

148 3. Superpixel segmentation

149 3.1. Principle of a superpixel annotation pipeline

150 Superpixels are groups of pixels that are perceptually similar (Ren and Malik, 2003). Before
151 discussing different algorithms to determine these similar regions, we briefly outline the general
152 annotation procedure. The overall aim is to obtain a pixel-wise annotation for image data. The
153 process can be separated into two steps:

- 154 1. **Boundary identification:** superpixels are used to determine regions with similar proper-
155 ties to simplify boundary identification. Different algorithms consider different aspects of
156 similarity (see Sec. 3.2);
- 157 2. **Instance labeling:** the obtained superpixels are then annotated with a corresponding class
158 label, which is then assigned to all pixels within this superpixel.

159 A schematic example of the superpixel annotation process is provided in Fig. 3

160 Instead of providing a discrete representation of images, superpixels are better aligned with
161 image edges and largely reduce the image complexity (Vargas et al., 2014). As shown in Fig. 4
162 and pointed by Neubert (2015), if K represents the number of objects in the image, $P = m \times n$ is
163 the number of pixels of the input image where m, n is the height and width [in pixels] of the given
164 image, then for the number of superpixels N :

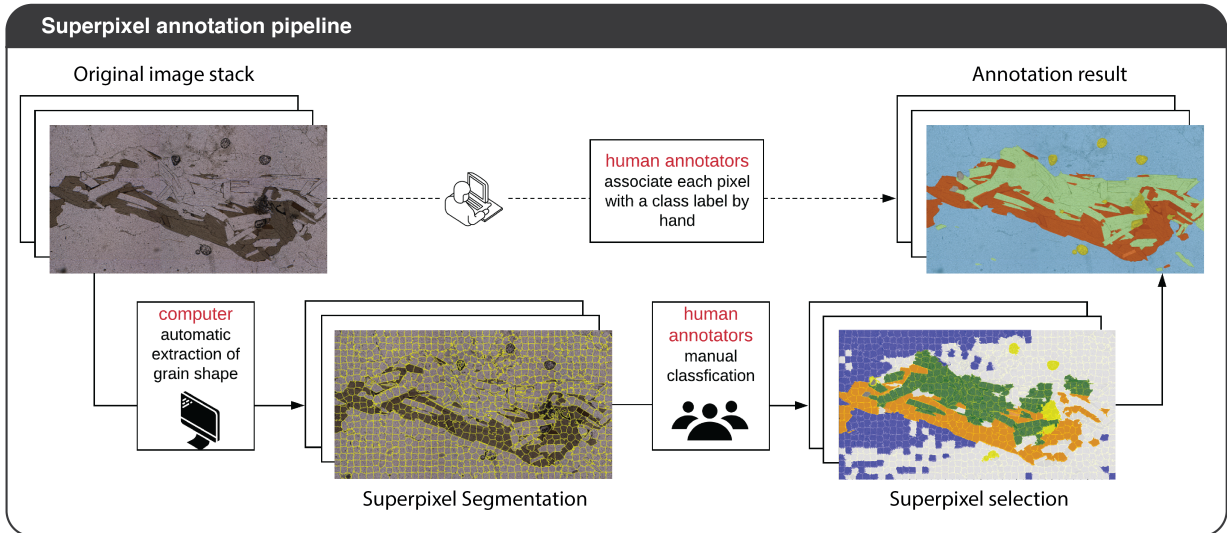


Figure 3: Superpixel annotation pipeline, indicated by solid lines: Given an image as input, superpixels are first extracted with an unsupervised algorithm. Human annotators will then associate superpixels with a corresponding class label. In the end, a pixel-wise annotation result can be obtained

$$K \ll N \ll P \quad (1)$$

165 A good superpixel segmentation, especially with a suitable detection of grain boundaries, has
 166 the potential to significantly reduce labeling time, but still leaves the possibility to include expertise
 167 through human annotators, leading to a good compromise for the generation of large thin-section
 168 training data sets.

169 3.2. Superpixel algorithms: state of the art

170 There are plenty of ways to generate superpixels. Here we briefly review the categorization of
 171 top performing recent algorithms according to the extensive investigation of superpixel algorithms
 172 performed by [Stutz et al. \(2018\)](#), Readers can gain a basic understanding of different approaches

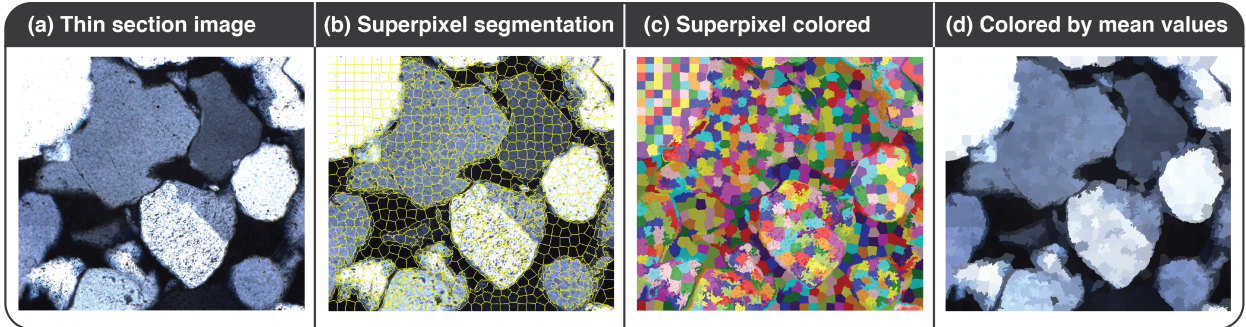


Figure 4: Example of a superpixel segmentation on an image of the Bentheimer sandstone (a) with a size of 1000x889 pixels, split into 811 superpixels (b). The segmentation result is visualized by yellow lines drawn on the original image. In the color-coded segmentation map (c), pixels belonging to the same superpixel have the same color. The mean color-coded map (d) shows average properties (here: color) in each superpixel.

173 from these categorizations without being perplexed by the implementation of each individual al-
 174 gorithm. The presented categorizations are graph-based, clustering-based, contour-evolution, and
 175 energy-optimization, which are based on the one proposed by [Achanta et al. \(2010\)](#) and extended
 176 by [Stutz et al. \(2018\)](#).

177 Graph-based algorithms treat an image as a weighted graph $G_w = (V, E, W)$ where each
 178 vertex $v_i \in V$ is associated to an image pixel i that is connected to an adjacent image pixel j by
 179 an edge element $e_k \in E$. $w_{ij} \in W$ is the edge weight representing the similarity between a pair
 180 of pixels i, j ([Neubert, 2015](#)). Based on the calculation of w_{ij} for each pair of nodes, the graph
 181 will be partitioned into disjoint regions. ERS ([Liu et al., 2011](#)) is a representative of graph-based
 182 algorithm.

183 Clustering methods are commonly used to find groups in observations. Probably the most well-
 184 known clustering algorithm is K -means ([Bishop, 2006](#)). K -means is simple, yet powerful. It is
 185 computationally fast and easy to implement. However, it has certain drawbacks, notably that the
 186 number of clusters K has to be defined beforehand. Moreover, the clustering result highly depends
 187 on the initial partitions ([Celebi et al., 2013](#)). Such dependence can be migrated by repeating the

188 clustering with different (randomized) initial cluster centers. There are many modifications and
189 variations of standard K -means proposed to address the problem regarding the initialization of
190 cluster (Celebi et al., 2013), and measure of Euclidean distance as intra-cluster metric (Park and
191 Jun, 2009; Velmurugan and Santhanam, 2010). Likewise, clustering-based superpixel algorithms
192 initialize seed pixels as “cluster centers” and measure color and spatial distance as within-cluster
193 metric (Stutz et al., 2018). Usually, the number of superpixels and their shapes and sizes can be
194 controlled over input parameters. A famous example of a clustering algorithm is SLIC proposed
195 by Achanta et al. (2010).

196 Contour evolution algorithms segment images by growing seed pixels such that the dilated
197 pixels adapt to local image structures (Stutz et al., 2018). Conceptually, they are rooted in the
198 early active contour model or snake method (Kass et al., 1988). The basic idea of the snake method
199 is to propagate or deform an initial contour surrounding the given object towards the boundary
200 of the detected object (Chan and Vese, 2001). The classic deformable contour model is built
201 on an energy functional that is specifically designed for smoothing and attracting contours. The
202 contour will stop evolving at boundaries where the energy functional can be minimized (Caselles
203 et al., 1997). However, snakes are not able to detect complex boundaries as they require an initial
204 contour beforehand. To address this problem, geometric active contour models based on curve
205 evolution approaches instead of energy minimization have been developed (Caselles et al., 1993
206 McInerney and Terzopoulos, 2000; Caselles et al., 1997). These models enable active contours to
207 handle changes in the topology during the curve evolution using a level-set method (Osher and
208 Sethian, 1988; Sethian, 1999). A recent example is ERGC (Buyssens et al., 2014b) generating
209 superpixels based on the eikonal equation.

210 Energy optimization algorithms start from an initial partition of images and progressively
211 refine the boundary pixels at each iteration (Conrad et al., 2013; Van den Bergh et al., 2012; Yao
212 et al., 2015a). Energy updating strategies ensure the connectivity of the final segmentation and
213 preserve the region topology in the image. The exchange of boundary pixels or the refinement of

214 boundary pixels is achieved by iteratively optimizing the energy function formulated for the image.
215 These algorithms differ in the selection of energy functions to be optimized as well as the strategy
216 of optimization; commonly used energy optimization algorithms are CRS (Conrad et al., 2013),
217 ETPS (Yao et al., 2015b) and SEEDS (Van den Bergh et al., 2012).

218 3.3. Qualitative evaluation of superpixel segmentation

219 When comparing superpixel segmentations, several aspects can be relevant. From an algorithm
220 in the context of mineral or grain segmentation considered here, we would expect to correctly
221 identify mineral or grain boundaries. This aspect is also related to the concepts of over- and
222 undersegmentation: Oversegmentation describes the effect that a single object (mineral or grain,
223 in our case) is segmented into more than one superpixel; whereas undersegmentation describes
224 that single superpixels contain more than one object. Clearly, oversegmentation is preferable, as
225 undersegmentation leads to a loss of information about the object boundaries. An additional aspect
226 to consider is the compactness of superpixels, i.e., how similar they are to a circle. Superpixels
227 with a very low compactness can have very thin and elongated shapes and then be difficult to select
228 in a post-processing step. All of these aspects will be considered and evaluated in the following
229 sections.

230 ¶ In a first step, we compare six state-of-art algorithms (Table A.1) recommended by Stutz
231 et al. (2018) and described in section 3.2. We apply all algorithms to the sandstone sample and
232 perform segmentations with different superpixel resolutions K ($K = 200, 400, 600, \dots, 3000$). The
233 additional settings for all algorithms are provided in table A.1 in the appendix.

234 A subarea of digital thin section for Bentheimer sandstone is selected for the experiment. It
235 contains 10 xpol image layers and 1 ppol layer with a uniform size of 1551x2171 pixels. Examples
236 of superpixel segmentations using the aforementioned algorithms are shown in Fig. 4, with maps
237 of superpixels (yellow lines) on a part of the thin section and superpixel maps with random col-
238 ors to show distribution and superpixel shape. There is no single best algorithm that can fit all

239 purposes. We observe that none of the algorithms can fully capture all boundaries when the super-
240 pixel density is low. The ability of all algorithms to capture boundary details increases for larger
241 numbers of superpixels. SEEDS and ETPS generate highly irregular superpixels compared to the
242 other algorithms, in this case this becomes clearly visible when K becomes 800. In comparison to
243 SEEDS and ETPS, CRS, ERGC and ERS generate relatively compact superpixels (i.e., superpix-
244 els approaching a spherical shape) with $K=25$ and less irregularly shaped superpixels at higher
245 superpixel density levels. Only SLIC can maintain a regular oversegmentation regardless of super-
246 pixel density, while resulting in compact superpixels and these features motivate the adaptation
247 of SLIC to the specific aspects of thin section data sets in the following.

248 3.4. MultiSLIC

249 Segmenting thin section data sets requires specific considerations that are different from other
250 image segmentation tasks, as thin sections contain more than just a single image layers (see Fig. 2)a.
251 Due to the change of polarization mode, misorientations of mineral axes and extinction behavior
252 of anisotropic minerals, the single cross-polarised images can significantly differ from each other
253 in terms of color, brightness and visible rock texture, and all information should be considered
254 to obtain the best possible segmentation. Therefore, a superpixel algorithm to cope with this
255 additional dimensionality would be desirable.

256 In 2018 Stutz et al. (2018) conducted a detailed evaluation of 28 state-of-the-art superpixel
257 algorithms and showed that SLIC was performing among the best in regards to boundary adher-
258 ence and segmentation accuracy. We observed a similar behaviour in the qualitative evaluation,
259 presented above (Sec. 3.3). Considering that SLIC is a rather simple, yet very fast algorithm
260 that performs well on a variety of data as indicated by its high rank in the previously mentioned
261 benchmark, we chose SLIC as a candidate algorithm for an adaptation to the domain of thin
262 sections data sets, where one data set contains M images, corresponding to the total number of
263 cross-polarized image layers plus one plain-polarized image.

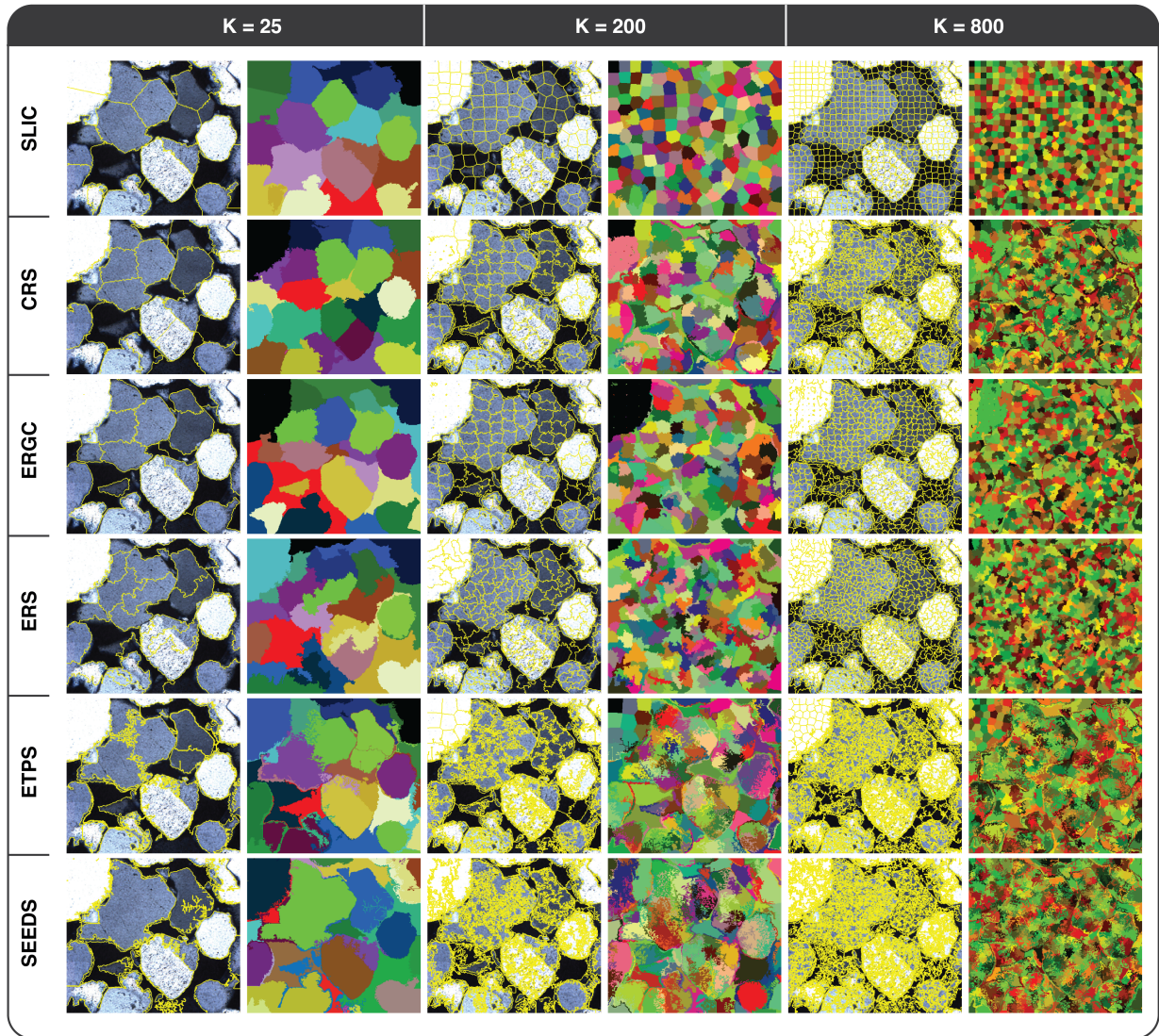


Figure 5: Example of superpixel segmentation results on an excerpt from the ViP data set of the Bentheimer sandstone. Superpixel boundaries are drawn in yellow, the corresponding random color coded segmentation masks are placed on the right. From left to right, images are shown for $K \approx 25$, $K \approx 200$, $K \approx 800$, respectively

264 For a better understanding of MultiSLIC, we provide here a brief description of the SLIC
265 algorithm, followed by a detailed implementation of MultiSLIC.

266 The *Simple linear iterative clustering* algorithm (SLIC) as proposed by Achanta et al. (2010) is
267 a superpixel algorithm that clusters pixel based on their spatial distance and color similarity. SLIC
268 is, in principle, a special case of *k-means* that initialises the k cluster centers $C_k = [l_k, a_k, b_k, x_k, y_k]^T$
269 at a regular grid interval S and uses a novel distance measure D on the 5D $[labxy]$ space. Here
270 $[x, y]$ stands for the coordinate plane and $[l, a, b]$ for the CIELAB color space. The grid interval S
271 is given by the number of pixel N and the number of cluster center k as $S = \sqrt{N/k}$.

272 Since all K superpixel should be approximately equally-sized, each should contain approximately
273 S^2 pixels. In the SLIC algorithm, the assumption is taken that any possible member pixel of a
274 superpixel lies within a $2S \times 2S$ neighbourhood of its center. Accordingly, instead of calculating
275 the distances for every pixel to every center, as is usually done in *k-means*, in SLIC one only
276 calculates distances from pixels to cluster centers within this $2S \times 2S$ neighbourhood, and this
277 approach significantly speeds up the clustering calculation.

278 The distance measure D introduced by Achanta et al. (2010) is defined as $D = d_{lab} + \frac{r}{S}d_{xy}$.
279 Here, d_{lab} and d_{xy} are the euclidean distances on the color space and coordinate space respectively,
280 while r a weighting term influencing the compactness of the superpixel.

281 SLIC therefore segments the single input image into K approximately equally sized superpixels
282 that are positioned in a regular manner, with a time complexity of $O(N)$. There is however no
283 guarantee that each superpixel is connected. Depending on the application, it is therefore necessary
284 to enforce connectivity in a post-processing step which is simply done by giving each connected
285 area its own label.

The general operating principle of MultiSLIC is practically identical to SLIC. To accommodate

the multidimensional input, the distance measure D_s differs from SLIC as follows:

$$\begin{aligned}
 d_{lab}^m &= \sqrt{(l_k^m - l_i^m)^2 + (a_k^m - a_i^m)^2 + (b_k^m - b_i^m)^2} \\
 d_{xy} &= \sqrt{(x_k - x_i)^2 + (y_k - y_i)^2} \\
 D_s &= \sqrt[p]{\sum_m |d_{lab}^m|^p} + \frac{r}{S} d_{xy}
 \end{aligned} \tag{2}$$

286 where m denotes the specific dimension and therefore d_{lab}^m expresses the Euclidean distance between
 287 the CIELAB color of two pixel in the same m -th image. Thus D_s is the sum of the p -norm over
 288 the m separate color differences and the coordinate distance normalized by the initial regular grid
 289 step size S multiplied by a weighting factor r . The algorithm is described in more detail in the
 290 Algorithm [1](#) box.

291 Note that r and p are control variables. The former gives control over the compactness of a
 292 superpixel, while p influences the impact of dimensions with small color differences. For example,
 293 consider $p_1 = 1$ and $p_2 = \infty$, with p_1 the norm collapses into a simple sum over the dimensional
 294 differences in color, whereas with p_2 the norm is equal to the highest difference regardless of the
 295 other dimensions. Additionally, if there is only one dimension ($M = 1$) and the p -norm is chosen
 296 as $p = 1$, then MultiSLIC defaults to the original SLIC algorithm.

297 3.5. Visual comparison between SLIC and MultiSLIC

298 Fig. [6](#) shows the superpixels extracted by MultiSLIC as well as by its original version SLIC. Both
 299 algorithms can capture the most details in the background image when K is around 3000. However,
 300 SLIC cannot detect the boundaries of “hidden” grains appearing dark due to the extinction. In
 301 contrast, MultiSLIC can extract most of the important region boundaries across different layers
 302 into one superpixel segmentation merely with $K \approx 400$. Intuitively, MultiSLIC generates a quite
 303 satisfying segmentation according to visual inspection and outperforms SLIC when K is small.

Algorithm 1: MultiSLIC

input : Desired number of superpixel K and M images

output: A superpixel segmentation

- 1 Initialize cluster centers $C_k = [l_k^1, a_k^1, b_k^1, \dots, l_k^M, a_k^M, b_k^M, x_k, y_k]^T$ at regular grid steps
 $S = \sqrt{N/K}$.
 - 2 Move cluster centers to the neighbouring pixel with the lowest gradient position.
 - 3 **repeat**
 - 4 **for** $k \leftarrow 0$ **to** K **do**
 - 5 Calculate distance D_s (Eq: 2) to C_k for all pixel from a $2S \times 2S$ neighbourhood
 around C_k .
 - 6 Assign each pixel to the closest center.
 - 7 Recalculate cluster centers and corresponding residual error E .
 - 8 **until** $E \leq threshold$;
 - 9 Enforce connectivity.
-

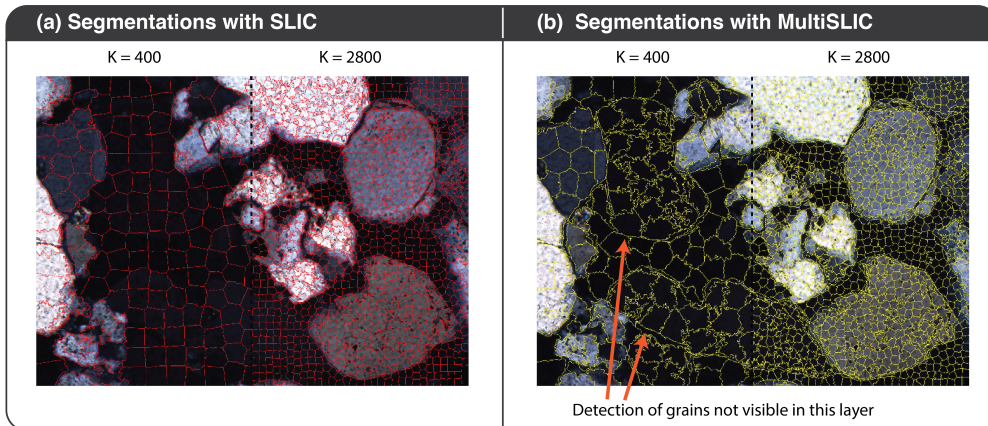


Figure 6: Qualitative result of segmentation generated by MultiSLIC. The same MultiSLIC superpixel segmentation is superimposed on xpol layer, In comparison, boundaries of SLIC superpixels are depicted as red. Each image contains two excerpts, the left and the right excerpt correspond to the result of $K \approx 400$ and $K \approx 2800$, respectively.

304 4. Quantitative evaluation of superpixel algorithms

305 After the visual inspection of the superpixel segmentation algorithms, we now compare the
 306 algorithms quantitatively. As ground truth, we use the boundary maps, generated by human
 307 annotators (Sec. 2.3).

308 4.1. Superpixel evaluation measures

309 Considering the high relevance of a precise boundary shape detection in the proposed human-
 310 computer collaborative annotation pipeline, we use boundary recall (Rec) (Martin et al., 2004)
 311 and undersegmentation error (UE) (Neubert and Protzel, 2012) to score the boundary adherence
 312 of superpixel segmentations generated by MultiSLIC and the set of recent advanced superpixel
 313 algorithms described in section 3.2. Given an image I with a total number of N pixels, let
 314 $S = \{S_1, \dots, S_m\}$ be the superpixel segmentation where m is the number of superpixels, and
 315 $G = \{G_1, \dots, G_n\}$ represents ground truth segmentations with n being the number of disjoint

316 partition of ground truth. The definitions of Rec and UE used in [Stutz et al. \(2015\)](#) are adopted
 317 here:

Boundary recall Rec is defined as

$$Rec(G, S) = \frac{TP(G, S)}{TP(G, S) + FN(G, S)} \quad (3)$$

318 where True Positives (TP) represent the number of boundary pixels in G correctly detected by
 319 boundary pixels in S within a certain tolerance. False Negatives (FN) are the number of boundary
 320 pixels in G for which no boundary pixels in S exists within a certain tolerance. [\(Stutz et al., 2018\)](#)
 321 suggested a local neighborhood h whose size is calculated as $h = (2r + 1) \times (2r + 1)$ with $r =$
 322 $0.0025 \times$ image diagonal as tolerance during the calculation. Rec assesses how well the superpixel
 323 boundaries align with the ground-truth edges.

The quantitative measure for the undersegmentation error UE , as proposed by [Levinshtein et al. \(2009\)](#), measures the fraction of superpixel leaks with respect to the ground-truth segmented border. A superpixel is supposed to align with the boundary of one object and UE punishes the superpixel segmentation if a superpixels boundary is crossing the boundary of a ground truth segment, meaning in other words the superpixel overlaps or leaks. As shown in [Fig. 7](#), superpixels are divided into in and out parts by a ground truth segment G . There are various ways to compute UE , [Levinshtein et al. \(2009\)](#) proposed to use the sum of “leakage” of superpixel S_j with respect to G as the undersegmentation error metrics. For example, this would be $(|B_{out} + C_{out} + D_{out}|) / |G|$ in [Fig. 7](#)

$$UE(G, S) = \frac{1}{N} \sum_{G_i} \sum_{S_j \cap G_j} \min \{|S_j \cap G_j, S_j - G_j|\} \quad (4)$$

324
 325 However, in such a way, superpixels that slightly cover the segments will be overly penalized.
 326 As a result, we adopt [Neubert \(2015\)](#)’s formulation expressed in [Eq. 4](#) when a superpixel is only
 327 slightly crossing a ground truth boundary, it will not affect the UE with the whole superpixel size,
 328 but only with the small overlapping part, in the example of [Fig. 7](#), that is $(|B_{in} + C_{out} + D_{in}|) / |G|$.

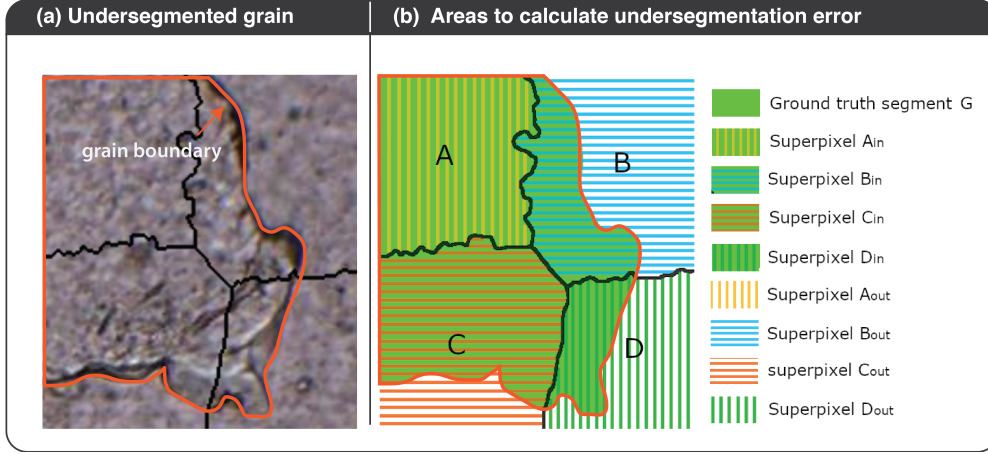


Figure 7: Illustration of undersegmentation error. The grain in the left input image is indicated by green ground truth segment that is split into four superpixels A, B, C, D in the right image.

One additional desiderata is compactness, a geometric property reflecting the regularity of a given shape as well as the boundary smoothness of the shape. Schick et al. (2012) suggested the use of an isoperimetric quotient (Osserman et al. 1978) to measure the compactness of the superpixel segmentation. The isoperimetric quotient $Q(S)$ is defined as the ratio of the area $A(S)$ of a superpixel S to a circle that has the radius of $\frac{P(S)}{2\pi}$:

$$Q(S) = \frac{A(S)}{\pi \left(\frac{P(S)}{2\pi}\right)^2} \quad (5)$$

where $P(S)$ is the perimeter of the superpixel. Q_s takes a maximum value of one for a circle and value $\pi/4$ for a square. Then the compactness of superpixel segmentation is defined as the average of isoperimetric quotient weighted by the size of superpixel compared to the whole image:

$$CO(G, S) = \frac{1}{N} \sum_{S_j} |S_j| Q(S_j) \quad (6)$$

329 Superpixel segmentations with a high CO are considered to be more compact.

330 4.2. Quantitative evaluation of superpixel segmentations

331 We will now evaluate how these previously described superpixel algorithms perform in a quan-
332 titative evaluation on the Bentheimer sandstone data set described above (Sec. 2.2). As the
333 conventional superpixel segmentation algorithms can only consider a single image, we compare the
334 measures on four different layers of the thin section data set:

- 335 • The image of plane polarized light (`ppol`)
- 336 • One image with cross-polarized light at angle 0 (`xpol_0`)
- 337 • An image with cross-polarized light at angle 144 (`xpol_144`)
- 338 • An image of maximum pixel intensity for all cross-polarized image layers (`max_intensity`)

339 The quantitative results with regards to boundary recall Rec are shown in Fig. 8. Since any
340 region where the pixel contrast is perceptually large is regarded as a boundary when generating
341 the ground truth boundary map, we suggest a threshold of $Rec \geq 95\%$ to be used for practical use.
342 It can be seen that all algorithms can refine the prior segmentation by increasing the number of
343 superpixels and generally lead to a good boundary recall. SEEDS is the top performer regardless
344 of the background images. SEEDS also grants an advantage at the very beginning when K is
345 small ($K=200$). Given either `max_intensity` layer or `ppol` layer as input image, ETPS offers a
346 competitive result with SEEDS especially for large K . CRS always yields a bad Rec for a lower
347 number of superpixels ($K \leq 400$) while quickly increasing the boundary adherence as K goes up
348 and finally its Rec reaches a value that is as good as the one yielded by ETPS. The rest algorithms
349 fall behind SEEDS, ETPS and CRS. SLIC is the worst performer in terms of Rec as it always lies
350 lowermost in the figure when K is around 3000. In comparison to other algorithms, MultiSLIC
351 shows higher Rec when $K \leq 1000$ in most scenarios, but this advantage gradually disappears as
352 the superpixel density (K) increases.

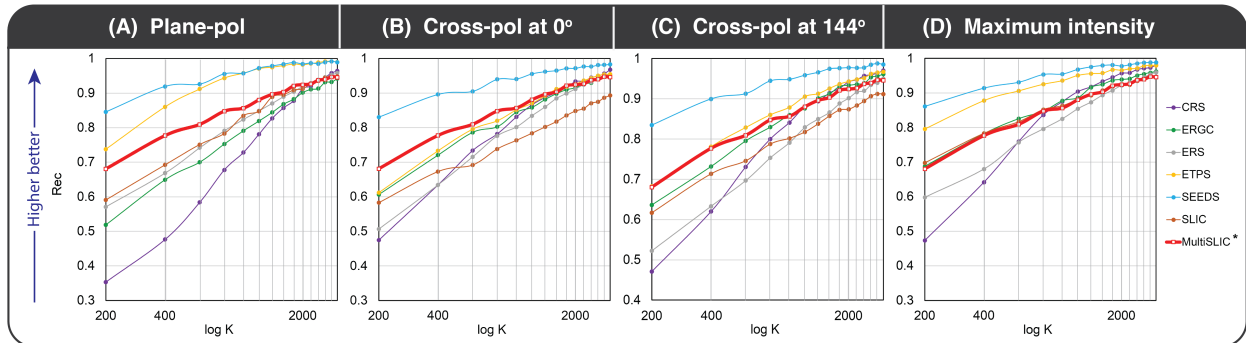


Figure 8: Averaged boundary recall of the resulting superpixel segmentations on four different information layers of BS. Rec is plotted as a function of superpixel density. K represents the number of superpixels, K varies from 200 to 3000 in steps of 200. A higher Rec means better boundary adherence.

353 Interesting to note is also that the variation of the input image does not seem to affect the
 354 relative performance of the tested algorithms. Although MultiSLIC cannot compete with the best
 355 performing algorithms with regard to Rec , it provides a stable and good Rec as compared to others
 356 and shows an advantage in Rec for CRS, ERGC, ERS and SLIC when K is small.

357 The undersegmentation error UE is a ground truth-dependent metric. Since UE measures the
 358 leakage of superpixels across the region boundaries in the given ground truth, it also provides
 359 an assessment of how tightly superpixels adhere to the boundaries. The quantitative results of
 360 UE are shown in Fig. 9. It is worth mentioning that undersegmentation exists in all superpixel
 361 segmentations. It is straight-forward to identify the top performer and bottom performer in terms
 362 of UE . MultiSLIC outperforms the rest of the algorithms, showing the lowest UE in all tested
 363 scenarios. Both ERS and SEEDS show a consistently high UE , no matter how input images vary.
 364 The remaining algorithms show moderate performance and approximate a similar UE for high
 365 numbers of superpixels K .

366 Rec and UE provide an overview of the algorithms' performances with respect to boundary
 367 accuracy. It is apparent that MultiSLIC provides considerably good performance regarding these

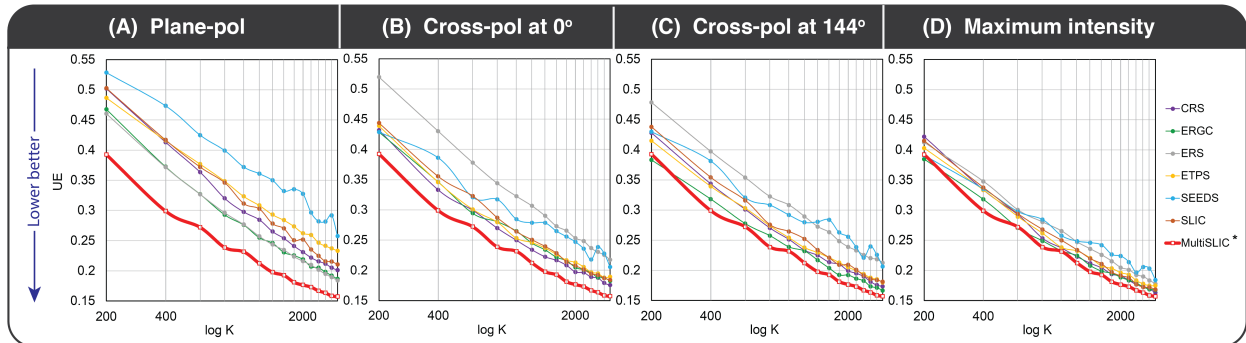


Figure 9: Quantitative results of the undersegmentation error. K represents the number of superpixels, K varies from 200 to 3000 in steps of 200. A lower UE means a better superpixel segmentation

368 two error metrics.

369 In addition to the performance in these measures, MultiSLIC generally results in compact
 370 superpixels. This aspect is illustrated in an evaluation of the compactness measures, shown in
 371 Fig. [10](#). Both SLIC and MultiSLIC generally create compact superpixels, especially for larger
 372 values of K , where other algorithms often start to generate thin and elongated superpixels (see
 373 also Fig. [5](#)). Both of them show a growing value of CO as the superpixel density is being increased.
 374 Also interesting to note is that SLIC performs worse on the `ppol` image, but better at others. This
 375 is likely to be related to the fact that MutliSLIC recovers more objects than SLIC and that,
 376 therefore, fewer domains without boundaries exist in the SLIC segmentation, leading to more
 377 compact superpixels—but at the cost of missing information (see also Fig. [6](#)).

378 Overall, MultiSLIC performs well on both a qualitative and quantitative level and can be
 379 used as a pre-segmentation algorithm dealing with the high dimensionality input from digital thin
 380 sections.

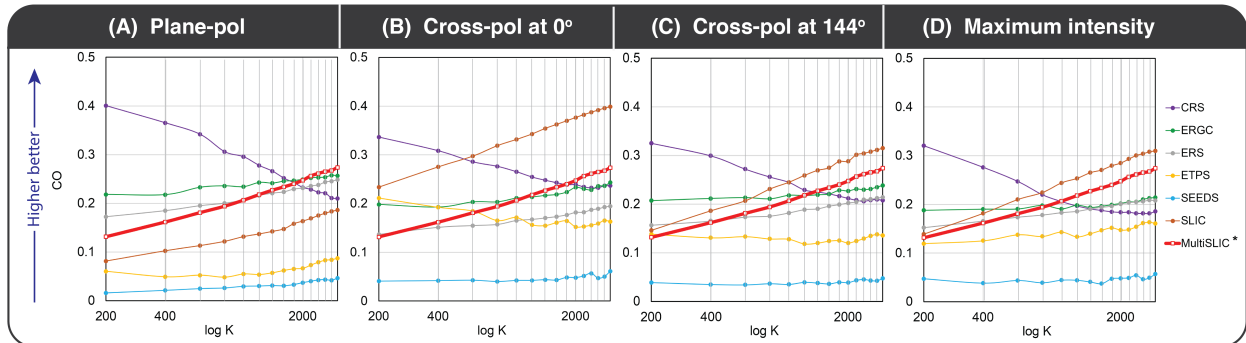


Figure 10: Compactness on four different information layers of the ViP data set. K represents the number of superpixels, K varies from 200 to 3000 in steps of 200. CO denotes Compactness. A higher CO represents that the shape of superpixel more resembles a circle.

381 5. Considerations for practical use

382 The presented superpixel methods, and specifically the developed extension to multiple channels
 383 in MultiSLIC, are only relevant when they support the main aim stated in the introduction:
 384 facilitating a faster generation of fully labeled thin section training data sets for machine learning
 385 applications. As a first test of feasibility to use these methods in a thin section labeling workflow,
 386 we developed a simple labeling tool and compared labeling efficiency to a standard boundary
 387 tracing approach.

388 5.1. Labeling tool

389 we developed a prototype labeling tool in Jupyter-notebook using Bokeh, an open source
 390 Python library that provides the possibility of customizing fully interactive apps for data analysis
 391 and visualization. As shown in Fig. 11, the labeling tool contains a viewer for displaying on the
 392 left and a output window showing the labeling result on the right. This simple app is easy to use
 393 and can be plugged in new functionality and interactivity according to the research demands. The

detailed implementation is accessible online [1](#)

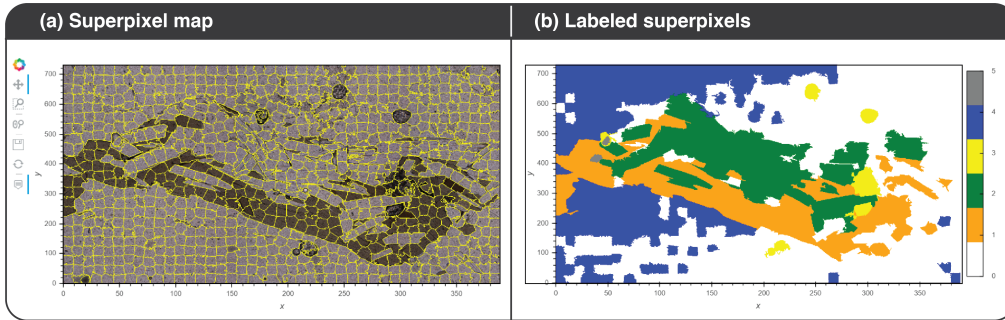


Figure 11: The interface of superpixel labeling tool in Jupyter-notebook

394

395 5.2. Notes on the efficiency of thin section annotations with superpixels

396 In order to identify the efficiency of the annotation pipeline, we performed two experiments
397 using the same digital thin section. The result were evaluated on a pixel-wise classified map with
398 same size as the input thin section, with approximately 80-90 grains(including sub-grains) in the
399 image. We compared the efficiency of the standard approach (boundary tracing) with a superpixel
400 approach:

- 401 • Experiment 1: Labeling the digital thin section using either a tablets and a stylus pen, using
402 standard labeling tools or graphics editors (QGis, PhotoShop).
- 403 • Experiment 2: Labeling the digital thin section using a MultiSLIC superpixel segmentation
404 with the labeling tool described above.

405 Timing results reported by the labeling experts indicated an increase of annotation speed by
406 a factor of 5 to 8. It can be expected that increasing the size of input image will make this time

¹<https://github.com/yujiixin666/Mineral>

407 difference bigger, as superpixels provide a full segmentation of the image into non-overlapping
408 segments.

409 Even if this is only a limited experiment, the results are very promising and suggest that
410 superpixel annotation methods can indeed be of very important use in the generation of fully
411 labeled thin section data sets, an important aspect of future work.

412 6. Discussion

413 Our results show that superpixel algorithms can efficiently segment thin section image data
414 sets, as an important step to generating training data sets for machine learning applications. This
415 aspect is especially relevant as thin section labeling requires expert knowledge, and this task can
416 therefore not simply be outsourced, for example over crowdsourcing platforms (e.g. Paolacci et al.
417 2010). Especially for the purpose of full image segmentation (see Fig. 1), these approaches therefore
418 open up the way to a generation of suitably large sizes of training data sets for a variety of machine
419 learning applications.

420 Thin section data sets also pose specific requirements to superpixel segmentation algorithms.
421 The most obvious aspect is that thin section data sets contain more than just a single image, due to
422 the combined use of plane-polarized light views and cross-polarized views at different angles. This
423 aspect is important, as superpixel algorithms are developed for classical image data sets (Stutz
424 et al., 2018). Due to this limitation, we implemented the extension of an existing algorithm, SLIC,
425 to use multiple image layers, resulting in the adapted algorithm MultiSLIC.

426 We evaluated several algorithms with respect to their successful use for the specific requirements
427 of thin section data sets. In Fig. 8 we showed the performance of tested superpixel algorithms
428 in terms of Boundary recall. According to the result, MultiSLIC cannot compete with SEEDS
429 and ETPS, both of them successfully detect more than 99% boundaries simply using a ppol layer.
430 However, an interesting observation can be obtained when analysing Fig. 8, 9, and 10 together:
431 SEEDS show the highest *Rec*, especially for large superpixel density, but yields the worst *UE* at

432 the same time. A possible explanation is that SEEDS actually oversegments the image locally but
 433 undersegments the image globally. This can be illustrated by Fig. 12. SEEDS always generates
 434 highly irregular superpixels with complex boundaries in order to exhaustively detect the subtle
 435 changes in the image which is good for boundary recall, but at the same time leads to a dramatic
 436 decrease in compactness of superpixels. It can be noticed that the grain is wrapped by layered
 437 thin superpixels at the rims. ETPS also shows wrapping behaviour. In this context, SEEDS and
 438 ETPS merely provide high apparent *Recs* but are actually not as suitable as a superpixel extractor
 439 for practical use when compared to MultiSLIC. It is also worth mentioning that ETPS provides
 440 a solid trade-off between compactness and boundary adherence. As it keeps superpixels compact
 441 for relatively homogeneous regions, promoting also the extension of this algorithm to use multiple
 image layers in future work.

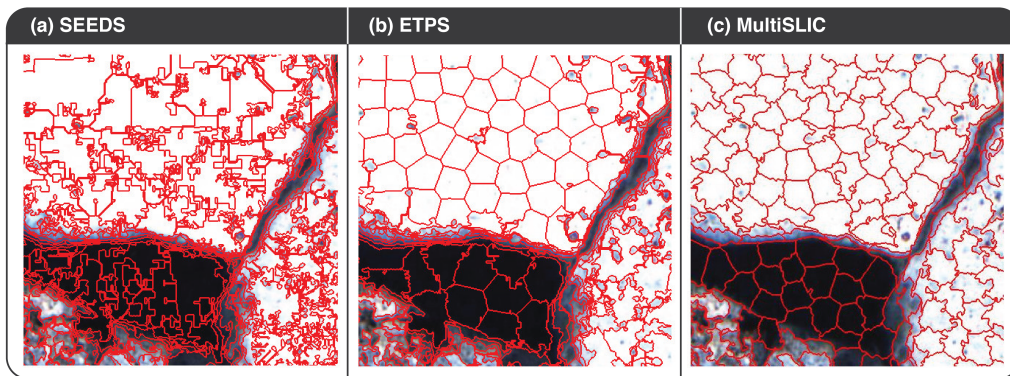


Figure 12: Zoom-in portions of segmentations generated by SEEDS, ETPS and MultiSLIC with superpixel density $K \approx 3000$.

442
 443 After generation of the superpixels, the next step in the annotation pipeline is the actual process
 444 of labeling. We demonstrate a simple example of a labeling tool above, but also a wide variety
 445 of tools exist for this purpose (Wigness, 2018; Anderberg and Liesén Gullmander, 2020). One
 446 additional post-processing step is to merge superpixels further according to similarity measures
 447 between superpixels.

448 A classical way to simplify the initial segmentation is to merge adjacent regions on the basis
449 of color similarity and spatial proximity (Trémeau and Colantoni, 2000). Region merging can be
450 carried out by constructing a map graph with each node associated with a region, and each pair of
451 adjacent regions are connected by an edge representing the relationship between adjacent regions
452 (Schettini 1993). This map graph is called Regional Adjacency Graph (RAG) that provides a
453 prior knowledge of image structure for region merging (Haris et al., 1998). For capturing the
454 redundancy of superpixel segmentations, each node in the RAG corresponds to one superpixel and
455 the edge between adjacent superpixels measures dissimilarity of their mean colors. Fig. B.14 shows
456 the construction of a RAG, the color of the edges indicates how dissimilar regarding mean color
457 two superpixels are. Brighter color means lower similarity. The edge would be black if adjacent
458 superpixels having the same mean color. Pairs of superpixels similar in color in the constructed
459 RAG will be progressively merged until no similar pairs remain. This is to say when a pair of
460 superpixels are merged, a new node is created. The weights of nodes adjacent to this merged node
461 will be recalculated and updated before proceeding to the next iteration.

462 Fig. 13 shows an example of RAG merging of the same superpixel segmentation using different
463 threshold values. The threshold is used to control the merging process. Edges with color dissim-
464 ilarity higher than the threshold will be retained. As shown in Fig. 13, using higher threshold
465 values will result in a more aggressive merging of superpixels. However, the result is sensitive
466 to the selection of threshold value. The efficiency of merging will be low if the threshold is too
467 small, higher threshold will cause the loss of important boundaries. Additionally, the calculation
468 of mean color for the set of pixels belonging to the same superpixel is highly dependent on the
469 given background image. Intuitively, a satisfied merging can be obtained by using a background
470 image with higher intensity contrast and vice versa.

471 We evaluated here the superpixel segmentation with a relatively simple data set, a thin section
472 of the Bentheimer sandstone. The internal structure of this rock type is rather simple, with quartz
473 as the dominating mineral and only low secondary alteration and limited differences grain shapes.

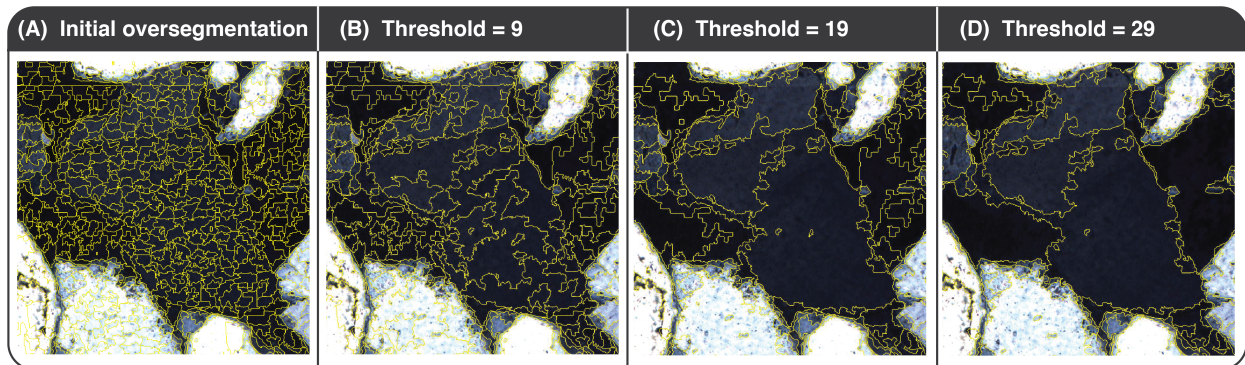


Figure 13: Result of RAG merging of initial superpixel segmentation using different threshold values. Using of higher threshold value will merge more superpixels.

474 In future work, it would be interesting to apply the best-performing algorithms to a variety of
 475 different rock types, for a detailed evaluation on segmentation of different rock types.

476 Superpixel segmentation results can be influenced by changing the input parameters to algo-
 477 rithms. The number of parameters for different algorithms varies from 2 to 6. However, it is
 478 impractical to exhaustively test all possible configurations of parameters. For a fair comparison,
 479 the default pre-optimized parameters according to [Stutz et al. \(2018\)](#) are used for each algorithm
 480 in the evaluation presented here. But such parameter selection cannot fully guarantee that the
 481 resulting segmentation for each implementation has the best quality, especially when considering
 482 other different types of rock.

483 7. Conclusion and Future works

484 In this paper, we proposed a human-computer collaborative pipeline to speed up the pixel-wise
 485 labeling of petrographic thin section images. In order to avoid subjective visual interpretations and
 486 hand delineations of the region boundaries, an algorithm will first splits images into superpixels.
 487 We have proposed a novel superpixel algorithm to cope with the high input dimensionality of digi-
 488 tal thin sections. Both qualitative and quantitative evaluation studies show the good performance

489 of MultiSLIC in terms of boundary adherence and compactness of the resulting segmentation.
490 Superpixels will then be labeled by human annotators with a specifically designed labeling tool.
491 Tests with different domain experts indicate a dramatic increase in labeling speed using the su-
492 perpixel labeling tool. Besides, the proposed pipeline has great generalization capacity allowing
493 wide collaboration for labeling petrographic thin section images at the pixel level. In the future we
494 will use the proposed pipeline integrated with the superpixel algorithm we developed to generate a
495 consistent and sufficiently large training data set with pixel-wise annotations that can be used to
496 develop novel ML and DL algorithms for intelligent analysis of petrographic thin section images.

497 **8. Acknowledgement**

498 The research in this project has been supported by the Exploratory Research Scheme of RWTH
499 Aachen University under the Exploratory Research Scheme Prep Fund Project "MINERALS:
500 Machine learning training set for virtual microscopy" (PFSDS023).

501 **Code availability section**

- 502 ■ • The code for superpixel segmentation (conventional methods) is available on [https://](https://github.com/davidstutz/superpixel-benchmark)
503 github.com/davidstutz/superpixel-benchmark.
- 504 ■ • Processing of results is performed with Jupyter notebooks, available on [https://github.](https://github.com/yujiixin666/Mineral)
505 [com/yujiixin666/Mineral](https://github.com/yujiixin666/Mineral)
- 506 ■ • A sample data set of the Bentheimer sandstone is available on [https://www.digitalrockportal.](https://www.digitalrockportal.org/projects/371)
507 [org/projects/371](https://www.digitalrockportal.org/projects/371).

508 **CRedit authorship contribution statement**

509 **Jiixin Yu:** Writing-Original draft, Formal analysis, Investigation, Visualization, Methodology,
510 Software and Data curation. **Florian Wellmann:** Writing-Review & Editing, Conceptualization,

511 Visualization, Supervision, Funding acquisition. **Simon Virgo:** Methodology, Data curation.
512 **Marven von Domarus:** Software, Validation **Mingze Jiang:** Data curation. **Joyce Schmatz:**
513 Resources, Funding acquisition. **Bastian Leibe:** Supervision, Funding acquisition.

514 **Appendix A. Parameters for superpixel algorithms**

515 **Appendix B. superpixel merging**

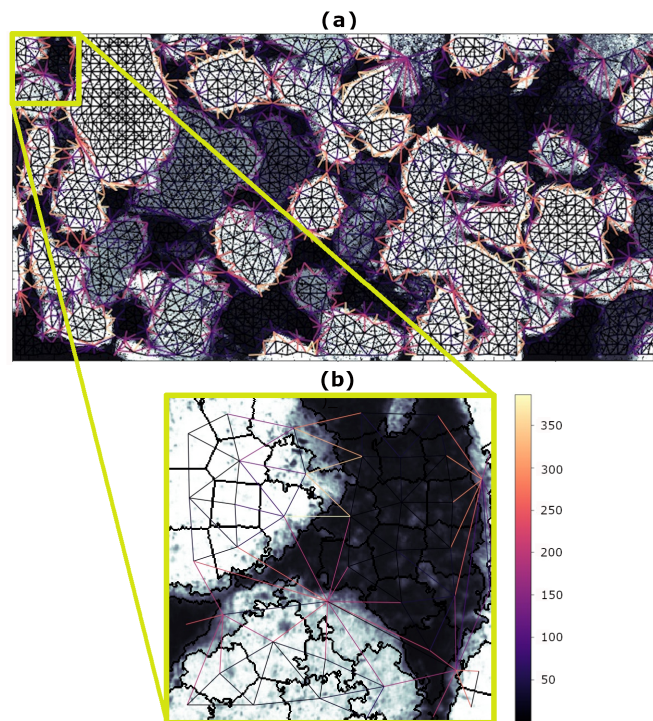


Figure B.14: Constructing Regional Adjacency Graph (RAG) for superpixel segmentation. (a) RAG for an oversegmentation of a sandstone image. (b) Zooming into the yellow outlined area where nodes and edges for superpixels are shown in detail.

Table A.1: Listing of superpixel algorithms and corresponding parameters used in each implementation.

Algorithm	Publication	Parameters	Categorization
Simple Linear Iterative Clustering (SLIC)	Achanta et al. (2012)	Compactness=10	Clustering-based
Contour Relaxed Superpixels (CRS)	Conrad et al. (2013) Mester et al. (2011)	Compactness=0.001 Cliques-cost=0.3 Iterations=3 Color space=0	Energy optimization
Eikonal Region Growing Clustering (ERGC)	Buyskens et al. (2014b) Buyskens et al. (2014a)	Color space=1 Perturb-seeds=0 Compacity =0	Contour evolution
Entropy Rate Superpixels (ERS)	Liu et al. (2011)	Lambda=0.5 Sigma= 5	Graph-based
Extended Topology Preserving Segmentation (ETPS)	Yao et al. (2015a)	Regularization Weight=0.01 Length weight=0.1 Size weight=1 Iterations= 25	Energy optimization
Superpixels Extracted via Energy-Driven Sampling (SEEDS)	Van den Bergh et al. (2012)	Bins=5 Prior=0 Confidence=0.1 Iterations=25 Color space=1 Means=1	Energy optimization

516 **References**

- 517 Achanta, R., Shaji, A., Smith, K., Lucchi, A., Fua, P., Süsstrunk, S., 2012. Slic superpixels
518 compared to state-of-the-art superpixel methods. *IEEE transactions on pattern analysis and*
519 *machine intelligence* 34, 2274–2282.
- 520 Achanta, R., Shaji, A., Smith, K., Lucchi, A., Fua, P., Süsstrunk, S., 2010. Slic superpixels.
521 Technical report, EPFL .
- 522 Anderberg, P., Liesén Gullmander, F., 2020. Annotation of image sequences using superpixels .
- 523 Baykan, N.A., Yilmaz, N., 2010. Mineral identification using color spaces and artificial neural
524 networks. *Computers & Geosciences* 36, 91–97.
- 525 Van den Bergh, M., Boix, X., Roig, G., de Capitani, B., Van Gool, L., 2012. Seeds: Superpixels
526 extracted via energy-driven sampling, in: *European conference on computer vision*, Springer.
527 pp. 13–26.
- 528 Bishop, C.M., 2006. *Pattern recognition and machine learning*. springer.
- 529 Borges, H.P., de Aguiar, M.S., 2019. Mineral classification using machine learning and images of
530 microscopic rock thin section, in: *Mexican International Conference on Artificial Intelligence*,
531 Springer. pp. 63–76.
- 532 Budenny, S., Pachezhertsev, A., Bukharev, A., Erofeev, A., Mitrushkin, D., Belozerov, B., et al.,
533 2017. Image processing and machine learning approaches for petrographic thin section analysis,
534 in: *SPE Russian Petroleum Technology Conference*, Society of Petroleum Engineers.
- 535 Buysens, P., Gardin, I., Ruan, S., Elmoataz, A., 2014a. Eikonal-based region growing for efficient
536 clustering. *Image and Vision Computing* 32, 1045–1054.

- 537 Buyskens, P., Toutain, M., Elmoataz, A., Lézoray, O., 2014b. Eikonal-based vertices growing and
538 iterative seeding for efficient graph-based segmentation, in: 2014 IEEE International Conference
539 on Image Processing (ICIP), IEEE. pp. 4368–4372.
- 540 Caselles, V., Catté, F., Coll, T., Dibos, F., 1993. A geometric model for active contours in image
541 processing. *Numerische mathematik* 66, 1–31.
- 542 Caselles, V., Kimmel, R., Sapiro, G., 1997. Geodesic active contours. *International journal of*
543 *computer vision* 22, 61–79.
- 544 Celebi, M.E., Kingravi, H.A., Vela, P.A., 2013. A comparative study of efficient initialization
545 methods for the k-means clustering algorithm. *Expert systems with applications* 40, 200–210.
- 546 Chan, T.F., Vese, L.A., 2001. Active contours without edges. *IEEE Transactions on image*
547 *processing* 10, 266–277.
- 548 Cheng, G., Guo, W., 2017. Rock images classification by using deep convolution neural network,
549 in: *Journal of Physics: Conference Series*, IOP Publishing. p. 012089.
- 550 Conrad, C., Mertz, M., Mester, R., 2013. Contour-relaxed superpixels, in: *International Workshop*
551 *on Energy Minimization Methods in Computer Vision and Pattern Recognition*, Springer. pp.
552 280–293.
- 553 Cordts, M., Omran, M., Ramos, S., Rehfeld, T., Enzweiler, M., Benenson, R., Franke, U., Roth,
554 S., Schiele, B., 2016. The cityscapes dataset for semantic urban scene understanding, in: *Pro-*
555 *ceedings of the IEEE conference on computer vision and pattern recognition*, pp. 3213–3223.
- 556 Deng, J., Dong, W., Socher, R., Li, L.J., Li, K., Fei-Fei, L., 2009. Imagenet: A large-scale hier-
557 archical image database, in: *2009 IEEE conference on computer vision and pattern recognition*,
558 Ieee. pp. 248–255.

- 559 Everingham, M., Van Gool, L., Williams, C.K., Winn, J., Zisserman, A., 2010. The pascal visual
560 object classes (voc) challenge. *International journal of computer vision* 88, 303–338.
- 561 Haris, K., Efstratiadis, S.N., Maglaveras, N., Katsaggelos, A.K., 1998. Hybrid image segmentation
562 using watersheds and fast region merging. *IEEE Transactions on image processing* 7, 1684–1699.
- 563 He, K., Zhang, X., Ren, S., Sun, J., 2016. Deep residual learning for image recognition, in:
564 *Proceedings of the IEEE conference on computer vision and pattern recognition*, pp. 770–778.
- 565 Hradiš, M., Kolář, M., Láník, A., Král, J., Zemčík, P., Smrž, P., 2012. Annotating images with
566 suggestions—user study of a tagging system, in: *International Conference on Advanced Concepts
567 for Intelligent Vision Systems*, Springer. pp. 155–166.
- 568 Iglesias, J.C.Á., Santos, R.B.M., Paciornik, S., 2019. Deep learning discrimination of quartz and
569 resin in optical microscopy images of minerals. *Minerals Engineering* 138, 79–85.
- 570 Karimpouli, S., Tahmasebi, P., 2019. Segmentation of digital rock images using deep convolutional
571 autoencoder networks. *Computers & geosciences* 126, 142–150.
- 572 Kass, M., Witkin, A., Terzopoulos, D., 1988. Snakes: Active contour models. *International journal
573 of computer vision* 1, 321–331.
- 574 Krasin, I., Duerig, T., Alldrin, N., Ferrari, V., Abu-El-Hajja, S., Kuznetsova, A., Rom, H., Uijlings,
575 J., Popov, S., Veit, A., et al., 2017. Openimages: A public dataset for large-scale multi-label
576 and multi-class image classification. Dataset available from <https://github.com/openimages> 2,
577 2–3.
- 578 Krizhevsky, A., Sutskever, I., Hinton, G.E., 2012. Imagenet classification with deep convolutional
579 neural networks, in: *Advances in neural information processing systems*, pp. 1097–1105.

- 580 Levinshtein, A., Stere, A., Kutulakos, K.N., Fleet, D.J., Dickinson, S.J., Siddiqi, K., 2009. Tur-
581 bopixels: Fast superpixels using geometric flows. *IEEE transactions on pattern analysis and*
582 *machine intelligence* 31, 2290–2297.
- 583 Lin, G., Shen, C., Van Den Hengel, A., Reid, I., 2016. Efficient piecewise training of deep structured
584 models for semantic segmentation, in: *Proceedings of the IEEE conference on computer vision*
585 *and pattern recognition*, pp. 3194–3203.
- 586 Lin, T.Y., Maire, M., Belongie, S., Hays, J., Perona, P., Ramanan, D., Dollár, P., Zitnick, C.L.,
587 2014. Microsoft coco: Common objects in context, in: *European conference on computer vision*,
588 Springer. pp. 740–755.
- 589 Liu, M.Y., Tuzel, O., Ramalingam, S., Chellappa, R., 2011. Entropy rate superpixel segmentation,
590 in: *CVPR 2011, IEEE*. pp. 2097–2104.
- 591 Long, J., Shelhamer, E., Darrell, T., 2015. Fully convolutional networks for semantic segmentation,
592 in: *Proceedings of the IEEE conference on computer vision and pattern recognition*, pp. 3431–
593 3440.
- 594 MacKenzie, W.S., Adams, A.E., Brodie, K.H., 2017. *Rocks and minerals in thin section: A colour*
595 *atlas*. CRC Press.
- 596 Maitre, J., Bouchard, K., Bédard, L.P., 2019. Mineral grains recognition using computer vision
597 and machine learning. *Computers & Geosciences* 130, 84–93.
- 598 Marmo, R., Amodio, S., Tagliaferri, R., Ferreri, V., Longo, G., 2005. Textural identification of
599 carbonate rocks by image processing and neural network: Methodology proposal and examples.
600 *Computers & geosciences* 31, 649–659.

- 601 Martin, D.R., Fowlkes, C.C., Malik, J., 2004. Learning to detect natural image boundaries using
602 local brightness, color, and texture cues. *IEEE Transactions on Pattern Analysis & Machine*
603 *Intelligence* 5, 530–549.
- 604 McInerney, T., Terzopoulos, D., 2000. T-snakes: Topology adaptive snakes. *Medical image analysis*
605 4, 73–91.
- 606 Mester, R., Conrad, C., Guevara, A., 2011. Multichannel segmentation using contour relaxation:
607 fast super-pixels and temporal propagation, in: *Scandinavian Conference on Image Analysis*,
608 Springer. pp. 250–261.
- 609 Młynarczyk, M., Górszczyk, A., Ślipek, B., 2013. The application of pattern recognition in the
610 automatic classification of microscopic rock images. *Computers & Geosciences* 60, 126–133.
- 611 Netzer, Y., Wang, T., Coates, A., Bissacco, A., Wu, B., Ng, A.Y., 2011. Reading digits in natural
612 images with unsupervised feature learning .
- 613 Neubert, D.I.P., 2015. Superpixels and their application for visual place recognition in changing
614 environments .
- 615 Neubert, P., Protzel, P., 2012. Superpixel benchmark and comparison, in: *Proc. Forum Bildver-*
616 *arbeitung*, pp. 1–12.
- 617 Osher, S., Sethian, J.A., 1988. Fronts propagating with curvature-dependent speed: Algorithms
618 based on hamilton-jacobi formulations. *Journal of computational physics* 79, 12–49.
- 619 Osserman, R., et al., 1978. The isoperimetric inequality. *Bulletin of the American Mathematical*
620 *Society* 84, 1182–1238.
- 621 Paolacci, G., Chandler, J., Ipeirotis, P.G., 2010. Running experiments on amazon mechanical turk.
622 *Judgment and Decision making* 5, 411–419.

- 623 Park, H.S., Jun, C.H., 2009. A simple and fast algorithm for k-medoids clustering. *Expert systems*
624 *with applications* 36, 3336–3341.
- 625 Peksa, A.E., Wolf, K.H.A., Zitha, P.L., 2015. Bentheimer sandstone revisited for experimental
626 purposes. *Marine and Petroleum Geology* 67, 701–719.
- 627 Ramil, A., López, A., Pozo-Antonio, J., Rivas, T., 2018. A computer vision system for identification
628 of granite-forming minerals based on rgb data and artificial neural networks. *Measurement* 117,
629 90–95.
- 630 Ren, X., Malik, J., 2003. Learning a classification model for segmentation, in: null, IEEE. p. 10.
- 631 Ronneberger, O., Fischer, P., Brox, T., 2015. U-net: Convolutional networks for biomedical image
632 segmentation, in: *International Conference on Medical image computing and computer-assisted*
633 *intervention*, Springer. pp. 234–241.
- 634 Russell, B.C., Torralba, A., Murphy, K.P., Freeman, W.T., 2008. Labelme: a database and web-
635 based tool for image annotation. *International journal of computer vision* 77, 157–173.
- 636 Schettini, R., 1993. A segmentation algorithm for color images. *Pattern Recognition Letters* 14,
637 499–506.
- 638 Schick, A., Fischer, M., Stiefelhagen, R., 2012. Measuring and evaluating the compactness of super-
639 pixels, in: *Proceedings of the 21st International Conference on Pattern Recognition (ICPR2012)*,
640 IEEE. pp. 930–934.
- 641 Sethian, J.A., 1999. *Level set methods and fast marching methods: evolving interfaces in computa-*
642 *tional geometry, fluid mechanics, computer vision, and materials science. volume 3.* Cambridge
643 university press.

- 644 Simonyan, K., Zisserman, A., 2014. Very deep convolutional networks for large-scale image recog-
645 nition. arXiv preprint arXiv:1409.1556 .
- 646 Singh, N., Singh, T., Tiwary, A., Sarkar, K.M., 2010. Textural identification of basaltic rock mass
647 using image processing and neural network. *Computational Geosciences* 14, 301–310.
- 648 Stutz, D., Hermans, A., Leibe, B., 2018. Superpixels: An evaluation of the state-of-the-art.
649 *Computer Vision and Image Understanding* 166, 1–27.
- 650 Sun, T., Zhang, W., Wang, Z.J., Ma, L., Jie, Z., 2018. Image-level to pixel-wise labeling: From
651 theory to practice., in: *IJCAI*, pp. 928–934.
- 652 Szegedy, C., Liu, W., Jia, Y., Sermanet, P., Reed, S., Anguelov, D., Erhan, D., Vanhoucke, V.,
653 Rabinovich, A., 2015. Going deeper with convolutions, in: *Proceedings of the IEEE conference*
654 *on computer vision and pattern recognition*, pp. 1–9.
- 655 Tang, D., Spikes, K., et al., 2017. Segmentation of shale sem images using machine learning, in:
656 *2017 SEG International Exposition and Annual Meeting*, Society of Exploration Geophysicists.
- 657 Thompson, S., Fueten, F., Bockus, D., 2001. Mineral identification using artificial neural networks
658 and the rotating polarizer stage. *Computers & Geosciences* 27, 1081–1089.
- 659 Trémeau, A., Colantoni, P., 2000. Regions adjacency graph applied to color image segmentation.
660 *IEEE Transactions on image processing* 9, 735–744.
- 661 Vargas, J.E., Saito, P.T., Falcao, A.X., De Rezende, P.J., Dos Santos, J.A., 2014. Superpixel-based
662 interactive classification of very high resolution images, in: *2014 27th SIBGRAPI Conference on*
663 *Graphics, Patterns and Images*, IEEE. pp. 173–179.
- 664 Velmurugan, T., Santhanam, T., 2010. Computational complexity between k-means and k-medoids

- 665 clustering algorithms for normal and uniform distributions of data points. *Journal of computer*
666 *science* 6, 363.
- 667 Virgo, S., Heup, T., Urai, J.L., Berlage, T., 2016. Virtual petrography (vip)-a virtual microscope
668 for the geosciences. EGUGA , EPSC2016–14669.
- 669 Von Ahn, L., Blum, M., Langford, J., 2004. Telling humans and computers apart automatically.
670 *Communications of the ACM* 47, 56–60.
- 671 Wigness, M., 2018. Superlabel: A superpixel labeling interface for semantic image annotation.
672 Technical Report. ARMY RESEARCH LAB ADELPHI MD ADELPHI United States.
- 673 Yao, J., Boben, M., Fidler, S., Urtasun, R., 2015a. Real-time coarse-to-fine topologically pre-
674 serving segmentation, in: *Proceedings of the IEEE conference on computer vision and pattern*
675 *recognition*, pp. 2947–2955.
- 676 Yao, J., Boben, M., Fidler, S., Urtasun, R., 2015b. Real-time coarse-to-fine topologically preserv-
677 ing segmentation, in: *Proceedings of the IEEE Conference on Computer Vision and Pattern*
678 *Recognition*, pp. 2947–2955.
- 679 Zhang, Y., Li, M., Han, S., Ren, Q., Shi, J., 2019. Intelligent identification for rock-mineral
680 microscopic images using ensemble machine learning algorithms. *Sensors* 19, 3914.